

# Microstructural Control of Weld Heat-Affected Zone of Steel by Mn Depletion around Non-metallic Inclusions

Shuji AIHARA\*<sup>1</sup>  
Masaaki SUGIYAMA\*<sup>2</sup>

Genichi SHIGESATO\*<sup>2</sup>  
Ryuji UEMORI\*<sup>3</sup>

## Abstract

*Role of Mn depleted zone formed around MnS precipitate in transformation of intra-granular ferrite (IGF) in low alloy steel subjected to simulated thermal cycle of weld heat-affected zone (HAZ) was studied. Mn distribution in austenite ( $\gamma$ ) adjacent to MnS were examined by field-emission type transmission electron microscope (FE-TEM) with energy dispersive X-ray spectroscopy (EDS). Foil samples for TEM were prepared using focused ion beam (FIB), which enabled a direct measurement of Mn concentration profiles near MnS. Change in area fraction of IGF with thermal cycle conditions was well explained by the extent of Mn depletion. It was concluded that the formation of IGF was controlled strongly by the Mn depletion effect in low alloy steels.*

## 1. Introduction

High-heat-input welding brings about significant advantages in costs and shortened working periods in the construction of welded steel structures such as ships and buildings. On the other hand, requirements for the safety and reliability of structures have grown more than ever over the last years, and it is necessary to secure high material toughness for preventing brittle fracture of steel members, especially in welded steel structures. Responding to such social requirements, Nippon Steel Corporation has developed steels for high-heat-input welding that have excellent toughness in weld heat-affected zones (HAZ), and has supplied such steels for a wide variety of applications such as ships, offshore structures, buildings and bridges<sup>1-3</sup>.

The toughness of the HAZ is governed by the properties of the iron matrix, a hardened phase acting as an initiation site of a crack and effective grain size<sup>4</sup>. In the HAZ of high-heat-input welding, the material is heated to high temperatures of 1673 K or higher, near the melting temperature of steel, for a long period, and as a result, grains coarsen remarkably. For this reason, preventing the increase in the effective grain size is especially important for improving the

toughness of a HAZ. Incidentally, the effective grain size is defined as the size of a region in which the crystallographic orientation of a body-centered cubic lattice is substantially the same.

In order to enhance the toughness of a HAZ by refining the effective grain size, it is effective to suppress the growth of austenitic ( $\gamma$ ) grains, refine the microstructure inside the  $\gamma$  grains or combine these two measures. To suppress the growth of the  $\gamma$  grains, it is very effective to pin their growth; particles of oxides and sulfides which are nanometer in size, contain elements such as Mg and Ca and are stable at high temperatures<sup>5,6</sup> are used for this purpose, in addition to conventionally used TiN particles<sup>7</sup>. On the other hand, to refine the microstructure inside  $\gamma$  grains, intra-granular ferrite (IGF) transformation is effective; TiN<sup>7</sup>, Ti<sub>2</sub>O<sub>3</sub><sup>8,9</sup>, TiN•Fe<sub>23</sub>(CB)<sub>6</sub><sup>10</sup>, TiN•MnS<sup>11</sup> and other oxides and precipitates have been reported as the particles that serve as the nuclei of the transformation.

While the mechanism of the IGF transformation has been discussed from such viewpoints as the lattice coherency between ferrite ( $\alpha$ ) and a particle and the formation of Mn-depleted zones in  $\gamma$  as a consequence to the precipitation of MnS<sup>12</sup>, the authors hypothesized that the formation of Mn-depleted zones plays an important role in the IGF transformation of a high-heat-input HAZ. The objective of

\*<sup>1</sup> Steel Research Laboratories

\*<sup>2</sup> Advanced Technology Research Laboratories

\*<sup>3</sup> Kimitsu R&D Labs.

this paper is to clarify the influences of Mn-depleted zones on the IGF transformation. For this end, the authors subjected an Al-killed low-alloy steel containing Ti to thermal cycles simulating various HAZs to investigate the IGF formation behavior, prepared specimens for transmission electron microscope (TEM) observation of non-metallic inclusions (hereinafter called simply the inclusions) that served as the sites of IGF formation employing a technique applying the focused ion beam (FIB) machining method, measured the Mn concentration around the inclusions in detail by the TEM-EDS (energy dispersive X-ray spectroscopy) analysis, and thus examined the mechanisms of the IGF transformation.

**2. Test Method**

A steel containing the alloying elements shown in **Table 1** was melted in a vacuum in the laboratory, cast into ingots, heated at 1,423 K for 3.6 ks and hot rolled into 15 mm thick plates. Then, test pieces for heat treatment 12 mm × 12 mm × 100 mm in size were cut out from those plates. The test pieces underwent the three thermal cycle patterns shown in **Fig. 1** in high-frequency induction heating equipment. Under the thermal cycle simulating the thermal history of a coarse-grain HAZ of high-heat-input welding, the test pieces were heated to 1,673 K and then cooled continuously to room temperature (curve C in Fig. 1). Under the other two thermal cycles (curves A and B in Fig. 1), the test pieces were heated to 1,713 K, then rapidly cooled to (A) 1,523 K or (B) 1,373 K within 5 s, held at the respective temperatures for 100 to 1,000 s, then rapidly cooled to 823 K within 5 s, held at the temperature for 30 s to have the α transformation occur, and then rapidly cooled to room temperature to freeze the transformation. All rapid cooling was done by He gas quenching.

A section of each test piece that went through one of the above thermal cycles was polished and etched with 2% nitral, and the microstructure was observed at the surface using an optical microscope to measure the area fraction of the IGF. The microstructure was observed just below the portion where a thermocouple was attached. After the measurement of the IGF area fraction, the inclusions serving as the sites of IGF formation were observed using a scanning electron microscope (SEM) and a TEM in the following three test pieces showing different IGF area fractions: Those heated

**Table 1 Chemical compositions of steel tested (mass%)**

C	Si	Mn	S	Ti	Al	N
0.08	0.19	1.47	0.004	0.012	0.026	0.004

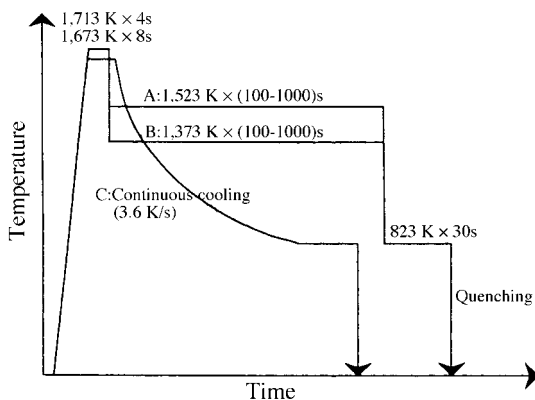


**Fig. 1 Simulated HAZ thermal cycle patterns**

to 1,713 K and then held at 1,373 K for (1) 100 and (2) 1,000 s, and (3) at 1,523 K for 1,000 s. The Mn concentration around the inclusions was measured using an EDS mounted on the TEM. After confirming inclusions that served as IGF formation sites through an SEM, thin film specimens of the inclusions for TEM observation were prepared by milling the inclusions into thin films by the FIB machining method using a FIB device, FB2000 made by Hitachi Ltd. A field emission type TEM (FE-TEM), HF2000 also made by Hitachi Ltd., equipped with a field emission type electron gun was used for the TEM observation and EDS analysis.

**3. Test Results**

**3.1 Thermal cycles and change of IGF area fraction**

**Figs. 2 and 3** show optical photomicrographs of the microstructures observed. Among the test pieces subjected to the thermal cycles to hold within the γ temperature range isothermally (curves A and B in Fig. 1), those held at 1,373 K for 100 s showed the largest amount of the IGF, and the IGF amount decreased as the holding time increased. The amount was smaller in the test pieces held at the higher holding temperature of 1,523 K. On the other hand, in the test pieces that were continuously cooled from 1,673 K, the IGF formed in more quantities than in those held within the γ temperature range. **Fig. 4** shows the IGF area fractions measured in these microstructures. The IGF fraction varied from 0 to 80% depending on the holding time and temperature, decreasing with longer holding time. The measure-

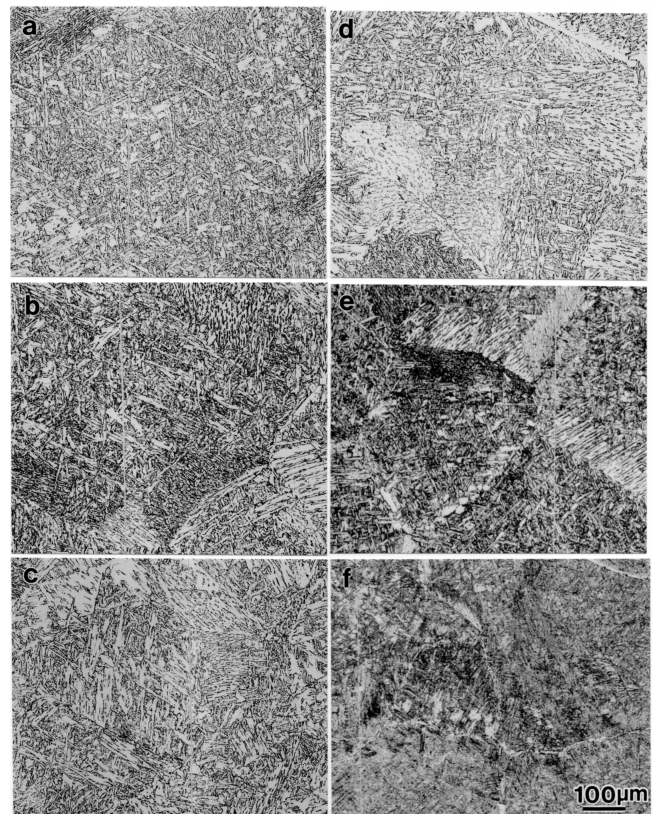


**Fig. 2 Microstructural changes with simulated HAZ thermal cycle conditions**

Held at (a)1,373K for 100s, (b)1,373K for 300s, (c)1,373K for 1,000s, (d)1,523K for 100s, (e)1,523K for 300s and (f)1,523K for 1,000s

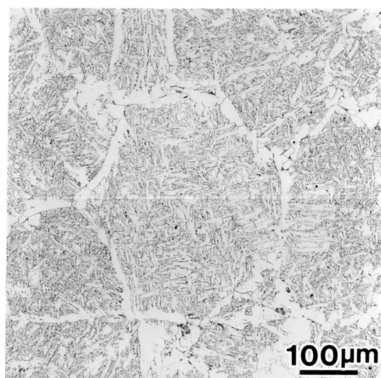


Fig. 3 Microstructure of continuously cooled specimen

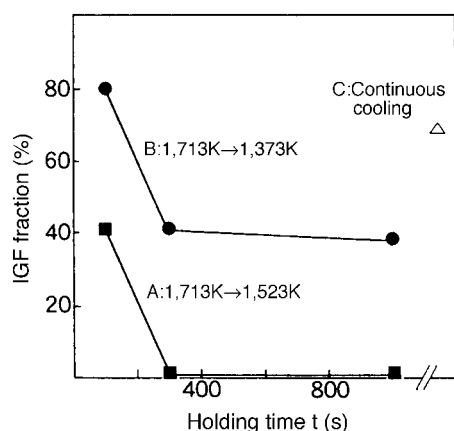


Fig. 4 Influence of holding time and temperature in austenite region on IGF area fraction

ment results showed that, while the IGF area fraction decreased only to approximately 40% after a holding at 1,373 K for as long as 1,000 s, it decreased to nearly zero after a holding at 1,523 K for only 300 s.

### 3.2 Mn concentration distribution around inclusions

Fig. 5 shows SEM micrographs of typical inclusions in a test piece heated to 1,713 K, then held at 1,373 K for 100 s (IGF area fraction approximately 80%) and another heated to the same temperature and then held at 1,523 K for 1,000 s (IGF area fraction 0%). In the test pieces of the former heat cycle, the IGF was found to form in quantities nucleating around  $Al_2O_3 + MnS + TiN$  composite inclusions. Fig. 5(a) shows such an example; IGF growing radially around an inclusion are indicated as F1 to F5.

In the test pieces of the latter heat cycle, on the other hand, the IGF was not found to form in spite of the existence of similar  $Al_2O_3 + MnS + TiN$  composite inclusions, and instead, martensite structure formed around the inclusions as a result of the rapid cooling from the  $\gamma$  temperature range (see Fig. 5(b)).

Figs. 6(a) and (b) show, respectively, an enlarged SEM image around the inclusion shown in Fig. 5(a) and a result of TEM observation of the same inclusion after machining the portion into a thin film specimen by the FIB method. Although Figs. 6(a) and (b) are SEM and TEM images of the same inclusion, the surface etching layer that had been formed at the SEM observation was removed during the preparation of the thin-foil, and as a result, its structure

suffered some modifications: For example, the  $Al_2O_3$  and TiN seen in the SEM image are missing in the TEM image. Nevertheless, it is clear that the inclusion (MnS) seen in the TEM image acted as the IGF nucleation site.

Fig. 7 shows the EDS measurement results of Mn concentration in steel around MnS inclusions. The abscissa represents the distance from the interface between MnS and ferrite ( $\alpha$ ), and ordinate the Mn concentration in the  $\alpha$  phase as measured by the EDS analysis. Here, the Mn concentration was measured at 10 points away from an interface by the same distance, and the average of the readings at the 10 points was used as the value of Mn concentration at the distance. The diameter of the beam used for the analysis was approximately 2 nm.

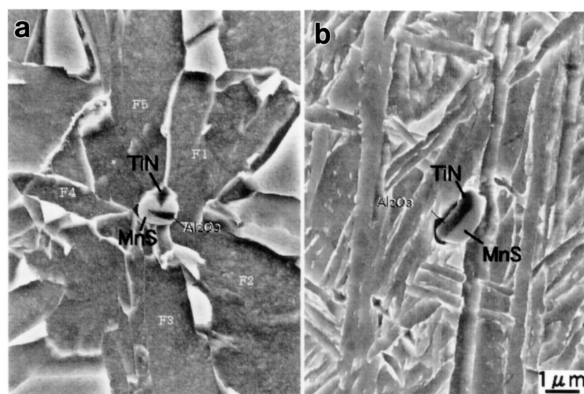


Fig. 5 Change in microstructure around an inclusion (SEM) with holding condition at austenite region, (a)1,373K for 100s, (b)1,523K for 1,000s

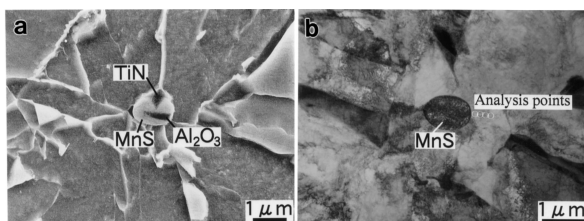


Fig. 6 IGF nucleated from an inclusion in the sample held at 1,373K for 100s, (a)SEM image, (b) TEM image

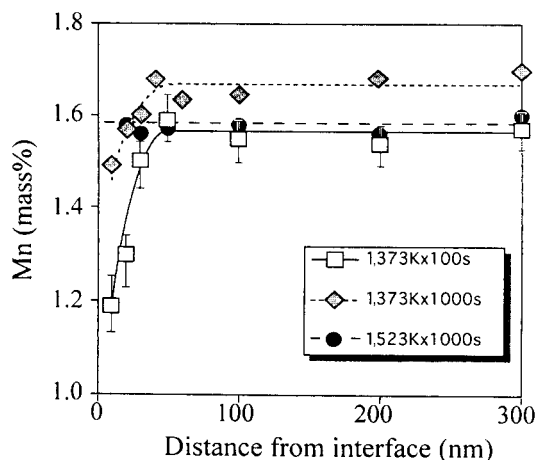


Fig. 7 Compositional profiles of Mn in steels adjacent to MnS

In the test pieces held at 1,373 K for 100 s (corresponding to Fig. 6), the nearer to the interface between MnS and the  $\alpha$  phase, the smaller the Mn concentration became; the Mn concentration in the region 10 nm from the interface was lower than that in regions sufficiently away from it by approximately 0.4 mass %. The decrease in the Mn concentration near the MnS- $\alpha$  interface was observed also in the test pieces held at 1,373 K for 1,000 s, but the decrease in the Mn concentration in the region approximately 10 nm from the interface (the difference from the value at points sufficiently away, roughly 200 to 300 nm, from the interface) was a little smaller, approximately 0.2 mass %. In contrast, in the test pieces held at 1,523 K for 1,000 s, the Mn concentration in steel did not decrease near the interface.

## 4. Discussion

### 4.1 Measurement accuracy of Mn concentration

The authors did not measure the Mn concentration at positions less than 10 nm from the interface. This is because it is impossible to set the MnS-Fe interface perfectly in parallel (edge-on) to the incidence direction of the electron beam. As a result, the fluorescent X-ray signal from the MnS could not be prevented from being detected at a position less than 10 nm from the interface. The reason why the interface could not be put edge-on to the electron beam is presumably that the interface was not flat, and that the portion of the inclusion fabricated into the thin-foil by the FIB technique was out of the center of the inclusion. Therefore, although the measurement results are thought to reflect the real Mn concentration distribution reasonably, there is still some room for improving the accuracy.

Incidentally, all the Mn concentration measurements at positions sufficiently away from the interface were substantially constant, fluctuating within an accuracy of  $\pm 0.03$  mass %, which indicates that the measurement accuracy was satisfactory. Counting error constitutes one of the factors that determine the accuracy of the EDS analysis. Letting a total number of counting be  $N$ , counting error  $S$  (%) is approximated as  $100 N^{-0.5}$ . The total number of counting of MnK $\alpha$  rays in the present test was 10,000 or more (total of the 10 points measured), and the counting error was approximately 1%. Therefore, assuming that the Mn concentration is 1.5 mass %, the concentration fluctuation caused by the counting error is approximately 0.015 mass %, which means that the above measurement accuracy is attainable. It has to be noted, however, that the Mn concentration at positions sufficiently away from an interface (the Mn concentration in the matrix phase) varied from specimen to specimen. That is to say, the Mn concentration in the matrix phase measured with different specimens cut out from test pieces that underwent the same thermal cycle fluctuated within the range from 1.5 to 1.7 mass % depending on the positions from which they had been cut out. This is presumably due to the fluctuation of the matrix Mn concentration owing to causes such as micro-segregation.

While the Mn concentration in the matrix phase varied specimen by specimen, it was substantially constant with little fluctuation within a specimen as written above, and thus the evaluation of Mn depletion was confirmed to be viable.

### 4.2 Verification of Mn-depleted zone formation by calculation

As described in the preceding section, the authors have confirmed through tests that the behavior of the Mn-depleted zone formation around an inclusion changes significantly depending on thermal history. They studied the issue further through calculation.

Since the concentrations of Mn and S were low, the authors assumed that the diffusion of these elements in a  $\gamma$  phase followed Fick's second law.

$$\frac{\partial C_{Mn}}{\partial t} = D_{Mn} \left( \frac{\partial^2 C_{Mn}}{\partial r^2} + \frac{2}{r} \frac{\partial C_{Mn}}{\partial r} \right) \quad (r_0 \leq r \leq r_{max}) \quad (1)$$

$$\frac{\partial C_S}{\partial t} = D_S \left( \frac{\partial^2 C_S}{\partial r^2} + \frac{2}{r} \frac{\partial C_S}{\partial r} \right) \quad (r_0 \leq r \leq r_{max}) \quad (2)$$

where:  $C_{Mn}$  and  $C_S$  are the concentrations of Mn and S (mass %), respectively;  $D_{Mn}$  and  $D_S$  are the diffusion coefficients of Mn and S in steel, respectively, which are functions of temperature  $T$  (K);  $t$  is time;  $r$  is a spherical coordinate having the origin as the center of an inclusion (MnS);  $r_0$  is the radius of the inclusion assumed to be spherical; and  $r_{max}$  is 1/2 of the average distance between inclusions.

Assuming that the solubility product of Mn and S are in equilibrium with MnS locally at an interface between MnS and a  $\gamma$  phase, then

$$\log_{10} (C_{Mn} C_S) = A - \frac{B}{T} \quad (r = r_0) \quad (3)$$

where  $A$  and  $B$  are constants. In addition, since the fluxes of Mn and S according to their respective concentration gradients during the precipitation or solution of MnS are equal to their stoichiometric ratio in MnS (1:1), the following equation holds true:

$$D_{Mn} \frac{\partial C'_{Mn}}{\partial r} \Big|_{r=r_0} = D_S \frac{\partial C'_S}{\partial r} \Big|_{r=r_0} \quad (4)$$

where  $C'_{Mn}$  and  $C'_S$  are the concentrations of Mn and S (mole fraction), respectively. Then, assuming that the boundary condition was expressed as

$$\frac{\partial C_{Mn}}{\partial r} \Big|_{r=r_{max}} = \frac{\partial C_S}{\partial r} \Big|_{r=r_{max}} = 0 \quad (5)$$

and that the Mn and S concentrations in a  $\gamma$  phase at 1,373 K were constant at 1.5 and 0.0001 mass %, respectively, as the initial condition, the solution and re-precipitation of MnS and the diffusion of Mn and S during the heating, cooling and holding processes were calculated solving equations (1) to (5) simultaneously. Here, in consideration of the S concentration in the specimen steel and the average radius of MnS of  $r_0 = 0.5 \mu\text{m}$ ,  $r_{max}$  was assumed to be  $10 \mu\text{m}$ . Note that, since the fluctuation of  $r_0$  was small, its value was assumed to be constant.

Figs. 8(a) and (b) show the calculation results for the two different holding temperatures, and Fig. 8 (c) shows the same for the continuous cooling. Here, the vertical axis represents the Mn and S concentrations in the  $\gamma$  phase, the horizontal axis the holding time at 1,523 (a) and 1,373 K (b), the axis in the depth direction the distance from the MnS- $\gamma$  interface. Whereas MnS dissolves during heating and the Mn and S concentrations near an inclusion rise as a consequence, MnS re-precipitates during cooling and the Mn and S concentrations near an inclusion fall, and thus zones depleted of these elements form around the precipitate.

When a steel material is held at 1,523 K (Fig. 8(a)), the fall of Mn concentration near the interface is small, approximately 0.1 mass % at the largest (after holding for approximately 50 s). Any longer holding time at the temperature decreases the fall of Mn concentration near a MnS- $\gamma$  interface further, and after approximately 500 s or more, the Mn concentration distribution becomes homogeneous irrespective of the distance from the interface. When a steel material is held at 1,373 K (Fig. 8(b)), on the other hand, the fall of Mn concentration near the interface is approximately 0.3 mass % at the largest (after holding for approximately 100 s). The relative decrease in Mn concentration near the interface is maintained through longer

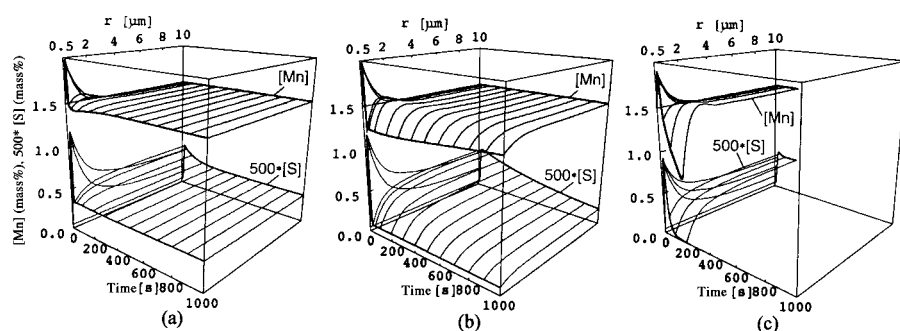


Fig. 8 Calculated Mn and S concentration in samples held at (a)1,523K, (b)1,373K, and (c)continuously cooled

holding time: after holding at the temperature for 1,000 s, the Mn concentration is still lower by approximately 0.2 mass %. In contrast, when a steel material is continuously cooled (Fig. 8(c)), since the solubility product of Mn and S decreases with temperature, the fall of Mn concentration near the interface increases.

#### 4.3 Mechanism of Mn-depleted zone formation

Table 2 shows the calculated and measured falls of Mn concentration near a MnS-matrix interface (hereinafter referred to as the Mn depletion) and the IGF area fractions under four heat treatment conditions. The Mn depletion, either calculated or measured, was obtained based on the Mn concentration at positions 10 nm away from an interface. It has to be noted that, whereas the calculated Mn depletion is that in the  $\gamma$  phase, the measured Mn depletion is that in the  $\alpha$  phase. However, since Mn diffuses little during a short holding time (30 s) at 823 K according to a calculation based on the diffusion coefficient of Mn in steel, one can judge that Mn concentration distribution is little different before and after the  $\gamma$ -to- $\alpha$  transformation, and thus, a direct comparison of the two figures is valid.

The formation of the Mn-depleted zones estimated on the bases of the diffusion equations of Mn and S and the assumption of the local equilibrium reasonably agrees with the measurement results of the EDS analysis using the FE-TEM. This indicates that the model used for the simulation calculation in the present test is capable of reproducing the actual formation processes of Mn-depleted zones pretty well. One can understand the influences of thermal history on the formation of the Mn-depleted zones and the Mn depletion as follows. (1) Because of the smaller diffusion rate of Mn than that of S, Mn-depleted zones form as MnS precipitates. (2) As the MnS precipitation advances, S is eventually consumed totally and MnS ceases to precipitate. Any longer holding time at the temperature results only in the diffusion of Mn, and the Mn-depleted zones disappear gradually. This is the reason why Mn depletion was small after a long holding time at 1,373 K. (3) When the temperature of holding is as high as 1,523 K, since the solubility product of Mn and S is large, MnS ceases to precipitate early and Mn diffuses rapidly thereafter, and as a consequence, Mn-depleted zones disappear within a short

time period.

#### 4.4 Mechanism of IGF formation

As seen in Table 2, the IGF area fraction is in close correlation with the Mn depletion around MnS, indicating that the Mn-depleted zones play an important role in the formation of the IGF. When discussing the IGF area fraction, it is necessary to take into consideration not only the IGF forming ability of individual inclusion particles but also the rate of cooling and the distribution (number density) of the particles. However, since the number density of inclusions was approximately 200 particles/mm<sup>2</sup> in the present test, little different from specimen to specimen, the authors considered the observed change of the IGF area fraction as described below, focusing only on the Mn depletion and cooling rate.

Mn is a  $\gamma$ -former; it is known that a decrease in Mn concentration in steel by 1 mass % raises the  $\gamma$ -to- $\alpha$  transformation temperature by approximately 50 K<sup>13)</sup>. For this reason, from the fact that Mn concentration was lower near MnS precipitates by approximately 0.4 mass %, one can surmise that the transformation temperature was higher there by approximately 20 K and the transformation began there in priority over other portions. In this case, however, it is necessary to take into consideration that, disregarding the influences of factors such as the decrease in the Mn concentration and lattice coherency, the commencement temperature of intra-granular transformation is lower than that of grain boundary transformation by 70 K or more<sup>9)</sup>, and for this reason, it is reasonable to suppose that the transformation commencement temperature is higher at  $\gamma$  grain boundaries than near a MnS precipitate inside a  $\gamma$  grain. By the heat patterns of the present test, the test pieces were rapidly cooled from the  $\gamma$  temperature range to 823 K, and the IGF is presumed to have formed near MnS simultaneously with a grain-boundary  $\alpha$  phase, resulting in an IGF fraction as high as 80%.

On the other hand, the fact that the Mn depletion of the test pieces that were held at 1,373 K for a long period decreased to a half seems to result from lower IGF transformation ability than that of the test pieces held at the temperature for a shorter period. One can presume that, in the test pieces that were held at 1,523 K, the Mn depletion

Table 2 Measured and calculated Mn depletion and IGF area fraction

Annealing condition	Mn depletion (measured)	Mn depletion (calculated)	IGF area fraction
1,373K for 100s	0.4mass%	0.3mass%	80%
1,373K for 1,000s	0.2mass%	0.2mass%	40%
1,523K for 1,000s	0mass%	0mass%	0%
Continuous cooling	-	0.6mass%	70%

decreased to zero, the transformation temperature shifted probably to significantly lower than 823 K, and as a consequence, only grain-boundary transformation occurred, resulting in the remarkable decrease in the IGF area fraction. By comparison, a low cooling rate leads to the transformation at  $\gamma$  grain boundaries in priority, resulting also in a low IGF area fraction. The reason why the IGF area fraction of the test pieces that were cooled continuously was not very high, approximately 70%, in spite of the large Mn depletion (calculated) of 0.6 mass % is presumably that the cooling rate was low and the transformation at  $\gamma$  grain boundaries proceeded in priority. This presumption is supported by the fact that the grain-boundary  $\alpha$  phase is seen in a comparatively large amount in the microstructure of a continuously cooled test piece shown in Fig. 3.

Another possible factor that influences the formation of IGF is that the presence of precipitates having high lattice coherency with an  $\alpha$  phase lowers the surface energy between the  $\alpha$  phase and the precipitates to accelerate the  $\alpha$  transformation. Whereas a confirmed fact is that, in middle-C steels, the  $\alpha$  phase that have nucleated around vanadium carbonitride particles is in such a specific orientation relationship with the vanadium carbonitride as to minimize misfit (the Baker-Nutting relationship)<sup>14</sup>, there is a paper reporting a case in which no such special orientation relationship existed<sup>15</sup>. TiN, which were found to form a part of the IGF formation nuclei in the present test, has the same B1 type crystal structure as vanadium carbonitride does, and is considered to have comparatively good lattice coherency with an  $\alpha$  phase.

However, if one assumes that TiN contributed to the formation of the IGF because of its good lattice coherency with the  $\alpha$  phase, then a specific orientation relationship between the IGF and TiN becomes a necessary condition for the IGF formation. What is more, since the IGF and a  $\gamma$  phase are in a K-S orientation relationship<sup>16</sup>, the above assumption leads to a conclusion that the IGF forms only from those TiN particles that have a specific orientation relationship with the  $\gamma$  phase. However, from the fact that, in the surfaces observed of the specimens of the present test having high IGF area fractions, the IGF was found to have formed from almost all TiN particles, the selective IGF formation because of the  $\gamma$ -IGF orientation relationship is little plausible. Furthermore, it is difficult to explain the results of the present test, in which the IGF formation behavior changed depending on the heating conditions in the  $\gamma$  temperature range, on account of the lattice coherency.

Ti oxides in steel are known to absorb Mn to form Mn-depleted zones<sup>17</sup>. Besides, there is a report pointing out that Mn-depleted zones formed around TiN particles leading to the formation of the IGF, without the mediation of MnS precipitates<sup>18</sup>. These indicate to the possibility that some Mn-depleted zone formation mechanisms different from those examined in the present test are involved in the IGF formation from Ti oxide particles. While the above requires further investigation in detail, Mn-depleted zones are considered to play an important role in the IGF formation from Ti oxide particles in the similar manner as observed in the present test.

## 5. Conclusion

- (1) The behavior of IGF formation nucleated from inclusions changed significantly depending on the temperature and time of holding in the austenite temperature range. The area fraction of the IGF decreased with longer holding time. In contrast, the IGF increased remarkably through continuous cooling.
- (2) The formation of Mn-depleted zones was confirmed through measurement of the Mn concentration distribution in austenite near MnS particles using TEM-EDS. The fall in the Mn concentration near an interface between MnS and austenite decreased with longer holding time in the austenite temperature range.
- (3) As a result of the calculation of the Mn concentration distribution in austenite resulting from the dissolution and precipitation of MnS, the calculated fall in the Mn concentration near the interface agreed well with the results of the measurement in (2) above.
- (4) The fall in the Mn concentration near an interface between MnS and austenite is in close correlation with IGF formation behavior, and a significant role in the IGF formation played by the formation of the Mn-depleted zones was confirmed.

## References

- 1) Aihara, S., Tomita, Y., Tsuzuki, T., Saito, N., Yoshida, Y., Ohkita, S., Imai, S.: OMAE99/MAT-2100
- 2) Chijiwa, R., Kojima, A., Tsuruta, T., Date, A., Isoda, S., Aihara, S., Saito, N., Ohkita, S., Imai, S.: OMAE99/MAT-2101
- 3) Kojima, A., Kiyose, A., Minagawa, M., Hirano, A., Yoshii, K., Nakajima, T., Hoshino, M., Ueshima, Y.: CAMP-ISIJ. 16, 360 (2003)
- 4) Mabuchi, H., Aihara, S.: *Materia*. 34 (3), 301-305 (1995)
- 5) Uemori, R., Koseki, Aihara, S., Hoshino, M., Matsubara, Y., Kojima, A., Terada, Y., Yoshida, Y., Minagawa, M., Funatsu, Y.: CAMP-ISIJ. 14, 1174 (2001)
- 6) Kojima, A., Kiyose, A., Uemori, R., Minagawa, M., Hoshino, M., Nakajima, T., Ishida, K., Yasui, Y.: *Shinnittetsu Giho*. (380), 2-5 (2004)
- 7) Kanazawa, S., Nakajima, A., Okamoto, K., Kanaya, K.: *Tetsu-to-Hagané*. 61 (11), 2589-2603 (1975)
- 8) Ohkita, S., Wakabayashi, M., Homma, H., Yamamoto, K., Matsuda, S.: *Seitetsu Kenkyu*. (327), 9-14 (1987)
- 9) Yamamoto, K., Matsuda, S., Haze, T., Chijiwa, R., Mimura, H.: *ASTM STP 1042*. 1989, p.266-284
- 10) Ohno, Y., Okamura, Y., Matsuda, S., Yamamoto, K., Mukai, T.: *Tetsu-to-Hagané*. 73 (8), 1010-1017 (1987)
- 11) Tomita, Y., Saito, N., Tsuzuki, T., Tokunaga, Y., Okamoto, K.: *ISIJ Int*. 34, 829-835 (1994)
- 12) Iron & Steel Institute of Japan: *Control of Transformation and Microstructure of Steels by Inclusions*. ISIJ, Tokyo, 1998, p. 929
- 13) Yamamoto, K., Hasegawa, T., Takamura, J.: *Tetsu-to-Hagané*. 79, 1169 (1993)
- 14) Ishikawa, F., Takahashi, T., Ochi, T.: *Metall. Master. Trans. A*. 25A, 929-936 (1994)
- 15) Yamaguchi, J., Takemura, N., Furuhashi, T., Maki, T., Uemori, R.: *CAMP ISIJ*. 11, 1128 (1998)
- 16) Shigesato, G., Sugiyama, M., Aihara, S., Uemori, R.: *CAMP-ISIJ*. 14, 1173 (2001)
- 17) Gregg, J.M., Bhadeshia, H.K.D.H.: *Acta metall. mater*. 42 (10), 3321-3330 (1994)
- 18) Shigesato, G., Sugiyama, M., Kojima, A., Shinohara, Y., Hara, T., Aihara, S., Takahama, K., Yamada, J.: *CAMP-ISIJ*. 16, 1532 (2003)